

# 3D Microstructure Segmentation by Topological Persistence

Anand V. Patel <sup>\*1</sup>, Tao Hou <sup>†2</sup>, Juan D. Beltran Rodriguez <sup>‡3</sup>,  
 Tamal K. Dey <sup>§2</sup>, and Dunbar P. Birnie, III <sup>¶1</sup>

<sup>1</sup>Department of Materials Science and Engineering, Rutgers University

<sup>2</sup>Department of Computer Science, Purdue University

<sup>3</sup>Department of Electrical and Computer Engineering, Rutgers University

## Abstract

Tomography is a widely used tool for analyzing microstructures in three dimensions (3D). The analysis, however, faces difficulty because the constituent materials produce similar grey-scale values. Sometimes, this prompts the image segmentation process to assign a pixel/voxel to the wrong phase (active material or pore). Consequently, errors are introduced in the microstructure characteristics calculation. In this work we develop a filtering algorithm based on topological persistence, a technique used in *topological data analysis*. One problem faced when evaluating filtering algorithms is that real image data in general are not equipped with the ‘ground truth’ information about the microstructure characteristics. For this study, we construct synthetic images for which the ground truth values are known. Specifically, we compare interconnected pore *tortuosity* and phase fraction. Experimental results show that our filtering algorithm provides a significant improvement in reproducing tortuosity close to the ground truth, even when the grey-scale values of the phases are similar.

**Keywords:** Tomography, Topological persistence, Image segmentation, Image filtering, Tortuosity

---

<sup>\*</sup>avp74@soe.rutgers.edu

<sup>†</sup>hou145@purdue.edu

<sup>‡</sup>jdb334@scarletmail.rutgers.edu

<sup>§</sup>tamaldehy@purdue.edu

<sup>¶</sup>dunbar.birnie@rutgers.edu

# 1 Introduction

Microstructures are the building blocks of a material: the shape, size, interconnection, and orientation of these microstructures play a key role in defining the ultimate properties and performance. For example, in energy storage systems like lithium ion batteries (LIB), these microstructures influence the ability to store energy, the conversion rates, and the diffusion phenomena [1, 2, 3, 4, 5, 6, 7]. Hence, analyzing and visualizing these microstructures help us understand the properties of the materials and design new materials [8].

Nowadays, microstructures are frequently examined in 3D using X-ray computed tomography (XCT or CT) [9]. In XCT, X-ray images are collected from many different directions and are interpreted to yield 3D maps of local X-ray absorption strength quantified by a grey-scale [10]. Besides an extensive usage of XCT in materials science to characterize fuel cell electrodes [11, 12], super-capacitor electrodes [13], porous ceramics [14], and fiber orientation in composites [15], XCT is also used in biological applications such as tumor detection [16, 17], fracture examination [18, 19], and blood clots [20]. In battery research, the XCT experiments are performed to measure three important microstructure characteristics, i.e., the porosity, the specific surface area, and the tortuosity of pore network [1, 21, 22].

For the present work, we emphasize microstructural tortuosity as it directly influences current flow rates within the interpenetrating electrolyte phase contained in the pores. Typically, before calculating porosity or tortuosity, the data gathered from XCT are post-processed to assign each voxel/pixel to the solid phase or the pore phase; this process is often called *image segmentation* (which means *binarization* for datasets of this paper). However, depending on the mixture of phases being studied and their ability to absorb X-rays, a ‘faithful’ binarization of data can be very difficult. In a binarization process, a threshold value is first picked by an algorithm such as the well-known Otsu’s algorithm [23] (henceforth called OTSU) and then any pixel/voxel above (resp. below) the threshold value is assigned active material (resp. porous region). OTSU algorithm finds a threshold value maximizing the variance between the two classes (black and white) and works well for images whose histograms have bimodal distribution (i.e., peaks of the two classes in the histograms are distinct). OTSU algorithm also has advantages such as not requiring prior knowledge of the input and having low computational cost. This is shown in Figure 1a, where the histogram of the grey-scale data has two distinct classes and the binarization by OTSU preserves almost all the important regions. However, due to its strong reliance on histograms, OTSU algorithm may have difficulty when peaks overlap and are not as distinguishable, as shown in Figure 1b. (We further note that in this case, no single threshold can completely reproduce a faithful segmentation of the input image.) In addition to this problem, data collected from XCT have artifacts, which can potentially clutter the grey-scale values of pixels/voxels [24, 25]. Hence, the motivation of this work is to improve the binarization results of images whose histograms have overlapping peaks.

Specifically, we propose a new filtering algorithm called PERSPLAT based on techniques developed from *topological data analysis* [26] (TDA). This algorithm exploits topological structures hidden in the data to filter out noise and speckle so that overlaps in the histogram can be reduced. The filtered data fed to OTSU afterwards can then have a better binarization result. Compared to traditional filtering algorithms (such as those described in [27, 28]), PERSPLAT algorithm has the following advantages:

1. Based on the theory of topological persistence [29], our algorithm detects *global* structures rather than local ones in a multi-scale manner. The removed noise can be of any shape which do not need to fit in a rectangular window. This is in contrast to traditional despeckling filtering algorithms [28] utilizing a moving window, which restricts the shapes of detected speckle.

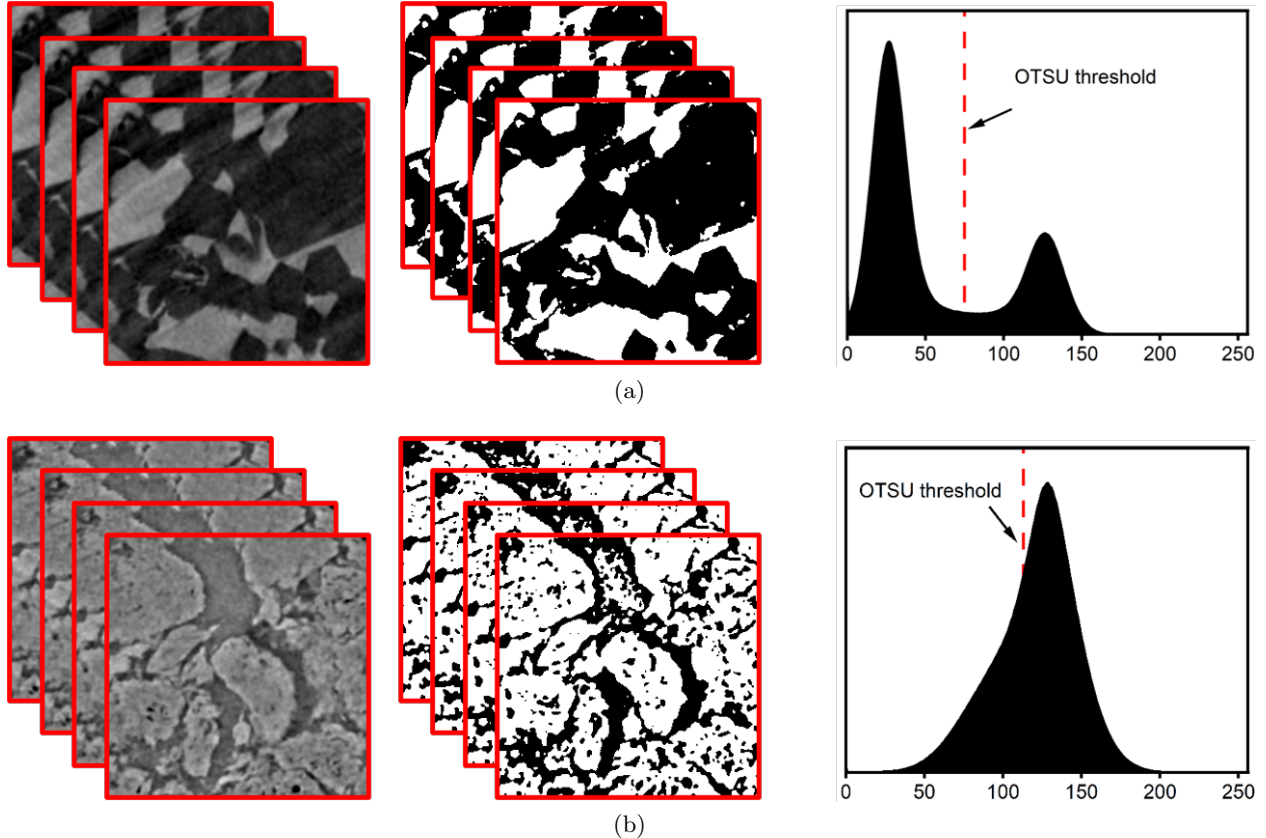


Figure 1: **XCT data.** (a) Grey-scale data, binarized data, and histogram of templated porous polymer. (b) Grey-scale data, binarized data, and histogram of commercial electrode.

2. In contrast to traditional despeckling or denoising algorithms [27, 28] which aim at recovering the ground truth image, our algorithm aims at a filtering of the image so that *the ensuing thresholding can recover the true segmentation of the two phases*. Achieving such a goal is especially valuable when the ground truth image is hard to binarize. As indicated by experiments, the two peaks of histograms for images can be successfully separated by our algorithm, so that the thresholding by a standard scheme (such as OTSU) is more reliable.
3. Some small but significant features can be preserved by inhibiting the removal of those small regions that *persist* for a long range of values. This is achieved with the help of the well-established tool called *barcodes* [26, 29] (or *persistence diagrams*), in which long *bars* are considered as significant features and short bars are treated as noise.

The absence of ground truth for the XCT data [30] makes it hard to compare the performance of various segmentation processes. Hence, to address the issue of ‘missing’ ground truth, we create synthetic images whose ground truth values are known. To justify the benefit of using PERSPLAT in conjunction with a standard binarization scheme (OTSU), we compare the computed tortuosity values with known ground truth values. As shown in Figure 2, our experiments demonstrate improvements achieved by using PERSPLAT; see Section 2 for details of our experiments.

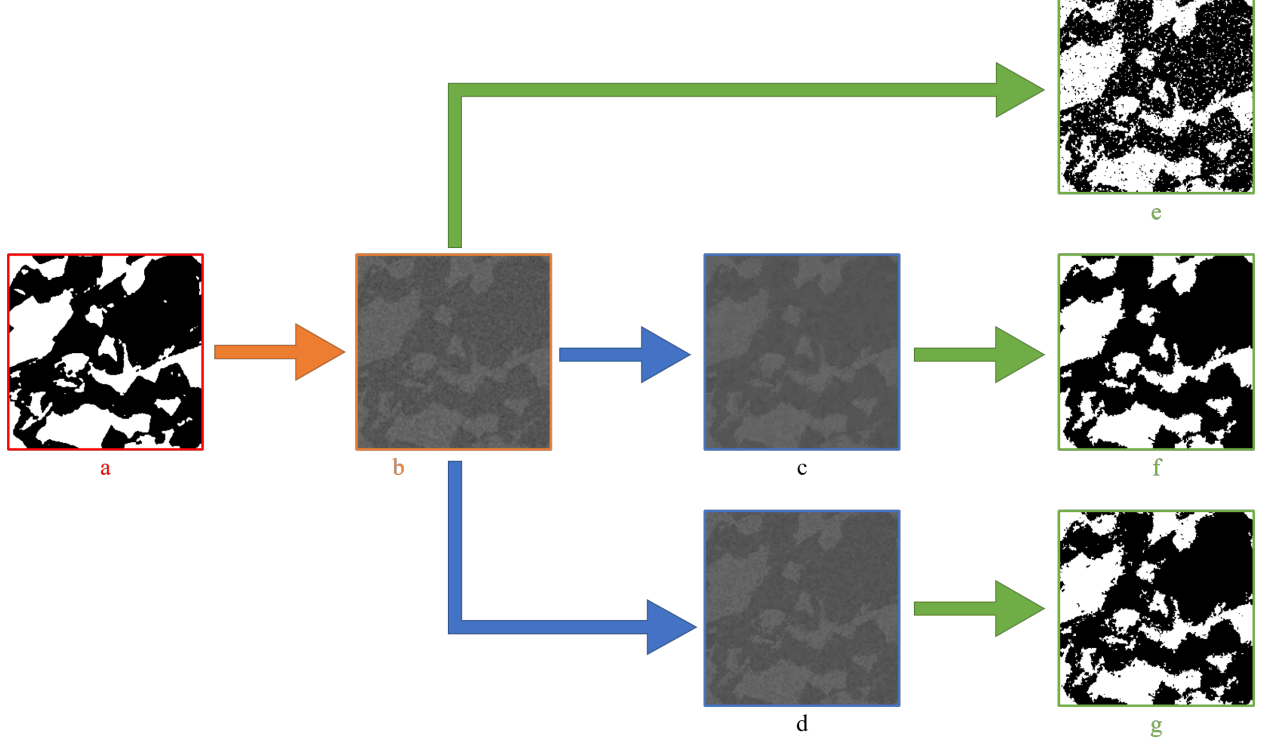


Figure 2: **Processing pipeline of the experiments.** (a) A ground truth slice of Synth1. (b) Synthetic image generated for the slice in (a). (c) Slice processed by PERSPAT-P. (d) Slice processed by PERSPAT-V. (e,f,g) Binarization results by Otsu.

## 2 Results and Discussion

**Synthetic dataset generation.** One of the main difficulties we face when evaluating a segmentation approach for XCT images is the absence of ground truth. To sidestep this problem, we synthetically generate datasets with known ground truth as follows:

1. Given a 3D XCT image, we first binarize the image with Otsu and *take this binarized image as ground truth*, i.e., those voxels with values greater than the threshold are in the solid phase and those with values less than are in the porous phase.
2. We then introduce synthetic noise to the established ground truth images based on Gaussian distribution, as explained further in Section 3. The introduction of Gaussian noises is justified by the fact that nearly all images we obtain through XCT have histograms akin to a mixture of Gaussians as shown in Figure 1.

**Experimental pipeline.** We apply our PERSPAT algorithm (detailed later) on 3D grey-scale images in two ways in this paper:

PERSPAT-P (i.e., PERSPAT-*Pixelized*): In this case, we process the 3D image *slice by slice* where the 3D input is treated as a stack of 2D pixelized slices. Each slice is processed with a version of PERSPAT tailored for 2D input. The outputs for all slices are then stacked to create a 3D filtered image.



PERSPLAT-V (i.e., PERSPLAT-*Voxelized*): In this case, *all slices together* are treated as a 3D voxelized image which is processed with a version of PERSPLAT tailored for 3D input. The output is also a 3D image.

To show the improvements on thresholding by using PERSPLAT, we adopt the following methods for binarizing our 3D input data (see Figure 2):

OTSU: This is the approach which directly uses OTSU for binarization.

PERSPLAT-P+OTSU: We first apply PERSPLAT-P for filtering the input and then use OTSU for binarization.

PERSPLAT-V+OTSU: This is the same as the previous method with the only difference that PERSPLAT-V is now used for the filtering.

After the binarization, we calculate the tortuosity for all binarized images using a MATLAB open-source application TAUFACTOR [31]. The tortuosity is then compared to the ground truth values.

In the rest of this section, we first give a brief introduction to the design of PERSPLAT so that readers can be better prepared for the experimental results detailed later. However, improvements introduced by using PERSPLAT can be easily seen even without a thorough understanding of the algorithm. For example, Figure 6 (presented later) shows that, with a properly chosen speckle size parameter (e.g., around 100), the tortuosity calculated from the PERSPLAT-P-filtered images is much closer to the ground truth than the tortuosity calculated from images binarized directly by OTSU. Note that speckle size is an input parameter to PERSPLAT which is explained later.

**PerSplat algorithm.** We only explain the algorithm in 2D and the 3D version follows similar steps. In 2D, we formalize the input image as a function  $f : G \rightarrow [0, M]$ , where  $[0, M]$  is an interval of integers with  $M$  usually equal to 255. Additionally,  $G$  is the graph corresponding to the 2-dimensional grid of an image, i.e., vertices of  $G$  correspond to pixels in the image and connect to either 4 or 8 of its neighbors.\* We also have that function values of  $f$  on the vertices are grey-scale values of the corresponding pixels.

For any  $s \in [0, M]$ , define  $f_s$  as the full subgraph of  $G$  containing vertices whose function values are no greater than  $s$ . We have that  $f_s$  is a subgraph of  $f_t$  whenever  $s \leq t$ . Therefore, starting from  $s = 0$ ,  $f_s$  keeps growing larger as  $s$  increases and eventually equals the entire  $G$ . For an  $s$ , we consider the *connected components* of  $f_s$ , i.e., those maximal sets of vertices of  $G$  in which each pair admits a connecting path. As we increase the value of  $s$ , the following three types of events can happen, in which we pay attention to the first and the third one (i.e., the *critical* events):

1. A new component in  $f_s$  which has no correspondence in  $f_{s-1}$  is *created*.
2. Components of  $f_{s-1}$  grow larger in  $f_s$ .
3. Several components of  $f_{s-1}$  *merge* into the same component in  $f_s$ .

The algorithm requires two parameters  $\mu$  and  $\lambda$  as inputs, where  $\mu$  denotes the *maximum speckle size* and  $\lambda$  denotes the *maximum persistence length* of a component that the algorithm can modify. Note that we always set  $\lambda = \infty$  in experiments so that the algorithm can modify any component.

---

\*In the experiments of this paper, our implementation of the algorithm always connects a vertex to 4 neighbors for 2D and 6 neighbors for 3D.

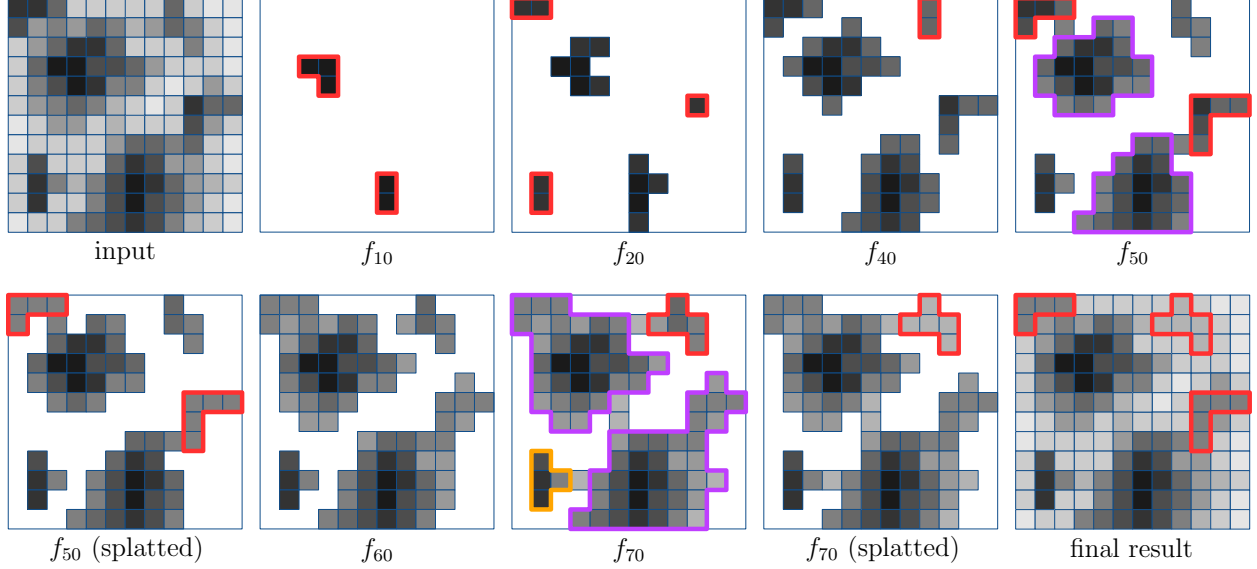


Figure 3: **An exemplar run of the first stage of PerSplat.** As  $s$  increases, connected components can be created (e.g., red ones in  $f_{10}$ ) or grow larger. The connected components can also merge among which some get splatted (e.g., red ones in  $f_{50}$ ) while some are preserved (e.g., purple and orange ones in  $f_{70}$ ).

The algorithm contains two stages, where the first stage increasingly enumerates  $s$  from 0 to  $M$ . During the first stage, whenever a merging happens at  $s$ , for each component  $C$  of  $f_{s-1}$  that merges with others, we define the following:

- Let  $|C|$  denote the *size* of  $C$ , which is the number of vertices of  $C$ .
- Let  $b(C)$  denote the *birth value* of  $C$ , which is the least function value of  $C$ 's vertices.
- Let  $\ell(C)$  denote the *persistence length* of  $C$ , which is defined as  $\ell(C) = |s - b(C)|$ .<sup>†</sup>

If  $|C|$  is no greater than  $\mu$  and  $\ell(C)$  is no greater than  $\lambda$ , we assign the value  $s$  to all pixels corresponding to the vertices of  $C$ , i.e., the component  $C$  is *splatted* to value  $s$  (see Figure 3). Note that the creation and merging of components actually construct the *merge tree* of  $f$ , which is a well-known tool in topological data analysis (TDA).

The second stage is a reverse process of the first: the value  $s$  is enumerated decreasingly from  $M$  to 0. Since the input image has been modified in the first stage, we let  $g : G \rightarrow [0, M]$  denote the function corresponding to this modified image. Furthermore, we define  $g^s$  as the full subgraph of  $G$  containing vertices whose function values (on  $g$ ) are no less than  $s$ . Therefore, as  $s$  decreases, connected components in  $g^s$  can also get created, grow, or merge with others. Note that birth value in this case is the greatest function value of the component. We then modify the pixel values for a component whenever a merging happens, which is similar to the previous stage.

Intuitively, the first stage suppresses those small “downward” (dark) bumps for the image and the second stage suppresses those small “upward” (bright) bumps. The parameters  $\mu$  and  $\lambda$  control how aggressive the suppressing is, in which trade-offs need to be made between noise filtering and possible loss of details. Figure 3 illustrates an exemplar run ( $\mu = 5$ ,  $\lambda = 30$ ) of the first stage, where

<sup>†</sup>Note that here we have an interval  $[b(C), s)$ . However, this interval is not exactly the same as an interval in a *persistence diagram* [26, 29], which does not produce an interval for the merged component with the least birth value.

the input image is considered to have six dark spots. Three smaller, less dark spots are splatted (i.e., turn to grey; see the red squares in the final result), leaving the remaining three spots which are more prominent preserved. In the exemplar run,  $f_{10}$  creates two connected components, while  $f_{20}$  and  $f_{40}$  create three and one component(s) respectively; the newly created components are marked by red squares. Note that these components are constantly growing after being created. In  $f_{50}$ , two pairs of components merge together in which the ones marked by red squares are splatted because of their sizes and persistence lengths. In  $f_{70}$ , all four components are merged where the one inside the red square is splatted; note that though the component inside the orange square has a size no greater than  $\mu$ , it is not splatted due to a longer persistence length than  $\lambda$ .

Finally, we observe the following property of PERSPLAT, which confirms the consistency of choices made to modify a component:

*For any node on the merge tree which is splatted by the algorithm, all its descendants are splatted. Equivalently, for any node which is not splatted, all its ancestors are not.*

**Overall results.** In our experiments, we generated synthetic datasets with different degrees of overlaps in the histograms based on different ground truths. To control histogram overlap, we adjust the mean and variance of the Gaussian distributions for the two phases (see Section 3 for details). Note that when the mean for the two phases is closer or the variance is larger, overlap in the histogram is more significant (see Figure 5 which shows histograms of synthetic datasets with various mean distances for the same ground truth).

Table 1 provides details of the generated synthetic datasets, where we list the data sources (i.e., the data samples from which we derived our ground truth), black phase fractions of the ground truth images, and the Gaussian parameters for the two phases. The ground truth for Synth1 and Synth2 was extracted from (different regions of) the XCT data of porous templated polymer. The ground truth for Synth3 and Synth4 was extracted from the tomographic data of a commercial LIB anode [1, 25]. The two sets of samples (i.e., porous polymer and LIB anode) were selected because of their difference in the phase fractions. Note that the histogram of Synth2 has more overlap than that of Synth1 based on Table 1; similar difference holds for Synth3 and Synth4.

Table 1: **Statistical setting for generated synthetic data.** The ground truth for Synth1 and Synth2 was extracted from porous polymer. The ground truth for Synth3 and Synth4 was extracted from LIB anode. Active material is assigned as white phase while porous region is assigned as black phase.

Dataset	Data source	Black phase fraction	White phase		Black phase	
			Mean	Var	Mean	Var
Synth1	porous polymer	66%	100	25	85	25
Synth2	porous polymer	75%	87	35	80	35
Synth3	LIB anode	35%	100	25	85	25
Synth4	LIB anode	35%	87	35	80	35

In Table 2, we show the tortuosity and the *binarization accuracy* (percentage of voxels correctly classified) calculated for the datasets listed in Table 1. We used the three methods mentioned earlier for binarization and underline the best values achieved. From Table 2, we observe that the best values for nearly all datasets were achieved by using PERSPLAT-P except Synth4 whose best tortuosity

Table 2: **Tortuosity and binarization accuracy calculated.** For each method, the speckle size  $\mu$  and the thresholding result by OTSU are provided. Tortuosity values closest to the ground truth and highest binarization accuracy are underlined.

Dataset	Method	Spec. size $\mu$	Thresh.	Tortuosity			Accuracy
				1	2	3	
Synth1	Ground truth	-	-	1.668	1.668	1.890	-
	OTSU	-	91	1.949	1.955	2.218	90.46%
	PERSPLAT-P+OTSU	54	92	<u>1.675</u>	<u>1.677</u>	<u>1.971</u>	<u>96.11%</u>
	PERSPLAT-V+OTSU	500	92	1.735	1.737	1.974	95.40%
Synth2	Ground truth	-	-	1.392	1.391	1.345	-
	OTSU	-	81	2.717	2.728	2.683	63.52%
	PERSPLAT-P+OTSU	54	82	<u>1.697</u>	<u>1.717</u>	2.392	<u>79.28%</u>
	PERSPLAT-V+OTSU	500	82	2.286	2.284	<u>2.256</u>	66.18%
Synth3	Ground truth	-	-	3.078	2.701	3.496	-
	OTSU	-	93	3.240	2.942	<u>3.441</u>	83.17%
	PERSPLAT-P+OTSU	54	93	<u>2.983</u>	<u>2.620</u>	3.763	<u>86.08%</u>
	PERSPLAT-V+OTSU	500	92	3.440	3.080	3.659	85.70%
Synth4	Ground truth	-	-	3.078	2.701	3.496	-
	OTSU	-	84	2.559	<u>2.532</u>	2.596	62.77%
	PERSPLAT-P+OTSU	54	84	2.148	2.109	4.310	<u>67.53%</u>
	PERSPLAT-V+OTSU	500	83	<u>3.046</u>	3.005	<u>3.101</u>	64.81%

values were achieved by using PERSPLAT-V. Therefore, results in Table 2 are consistent with our claim that PERSPLAT improves the thresholding quality of approaches like OTSU. Note that we fix speckle size  $\mu$  for all datasets when running PERSPLAT-P or PERSPLAT-V for comparison purposes; see experiments presented later in the section for influence of the  $\mu$  parameter on binarization.

Figure 2 illustrates the improvements on segmentation quality introduced by using PERSPLAT, where Figure 2a shows a 2D slice of the ground truth of Synth1 and Figure 2b shows the corresponding slice of Synth1 with synthetic noise. Using OTSU alone for segmentation resulted in a speckly image due to overlaps in the histogram (Figure 2e). In contrast, after using PERSPLAT-P and PERSPLAT-V for filtering (Figure 2c and 2d), the resulting images segmented by OTSU (Figure 2f and 2g) preserved the important regions with less speckle (see also Figure 5). Note that the segmented images in Figure 2f and 2g had fuzzier phase boundaries than the ground truth. This is an artifact introduced by the splatting of regions around the phase boundaries in PERSPLAT. However, the benefits of using PERSPLAT still greatly outweigh the artifacts introduced, considering that the major microstructures are recovered.

**Varying mean distance.** Lithium-ion battery electrodes usually contain polymeric based binders (for example Poly-vinylidene fluoride) to maintain the mechanical strength of the electrode during manufacturing and the (de-)lithiation process [21]. Since the binders are composed of low weight elements, during XCT they tend to absorb the X-rays which results in grey-scale values similar to an active material. As a consequence, the histogram tends to have overlap and form a single

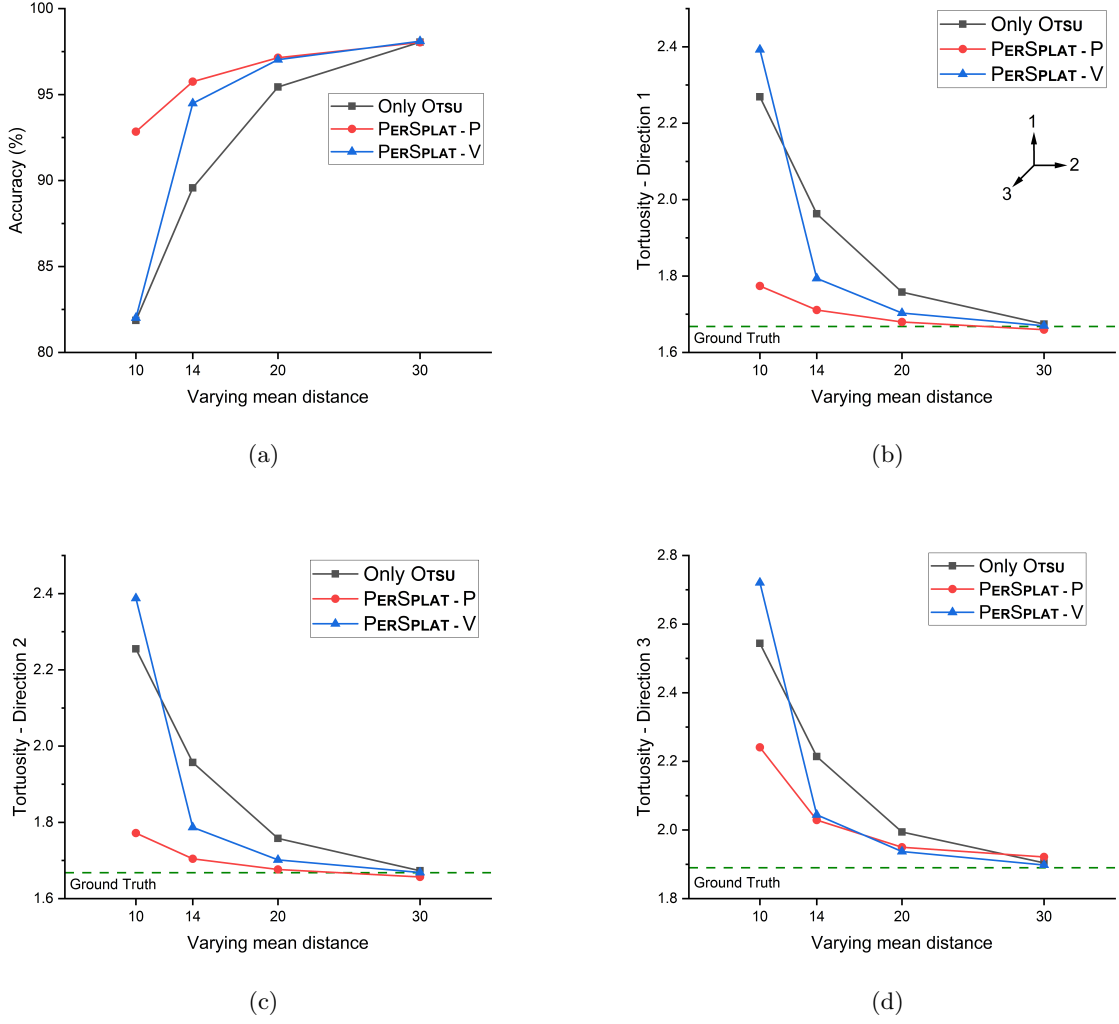


Figure 4: **Varying mean distance results.** (a) Binarization accuracy at various mean distances. (b-d) Tortuosity in the three directions at various mean distances.

peak. Binarization in such cases is hard. In view of this, we generated synthetic datasets with various degrees of histogram overlap for the same ground truth, to see how PERSPLAT aids OTSU binarization in the different scenarios. We controlled the histogram overlap by varying the mean distance from 10 to 30 as shown in Figure 4, while using the same standard deviation of 25 for all. Note that we simply denote the binarization method PERSPLAT-P+OTSU as PERSPLAT-P (similarly for PERSPLAT-V) in the figure, which should not cause any confusions.

From Figure 4, it is apparent that more histogram overlap (i.e., closer mean distance) resulted in more difficulty in binarization for all three methods, with the tortuosity turning further away from the ground truth. However, we can also see that PERSPLAT is constantly improving the binarization quality especially when the mean distance becomes close. For example, PERSPLAT-P filtering gives the best results in all measurements for the most difficult situation (mean dis. = 10).

Figure 5 shows slices from the input datasets as well as binarized ones from OTSU and PERSPLAT-P+OTSU. The figure also shows histograms of the input datasets and ones filtered

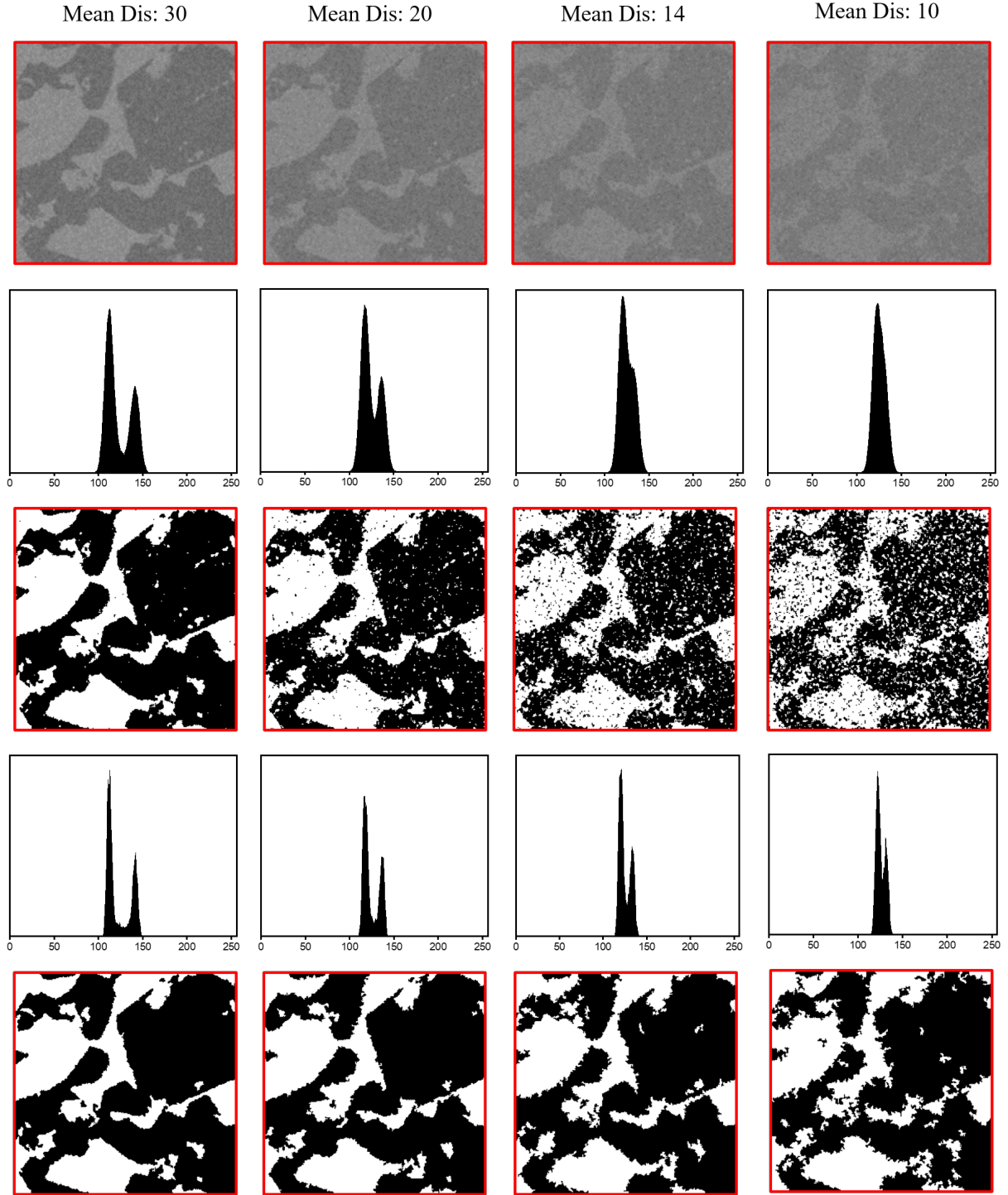


Figure 5: **Visual illustration for datasets with various mean distances.** From left to right, mean distance of the two phases for the synthetic noise decreases, resulting in more and more overlap in the histogram. Row one: one slice taken for each generated synthetic dataset. Row two: respective histograms of the datasets. Row three: respective binarized slices by applying OTSU only. Row four: respective histograms after applying PERSPAT-P. Row five: binarized images by PERSPAT-P+OTSU.

by PERSPAT-P. From the figure, we observe an interesting phenomenon: PERSPAT-P tends to separate the two peaks in histograms for the datasets which are otherwise cluttered in the original ones.

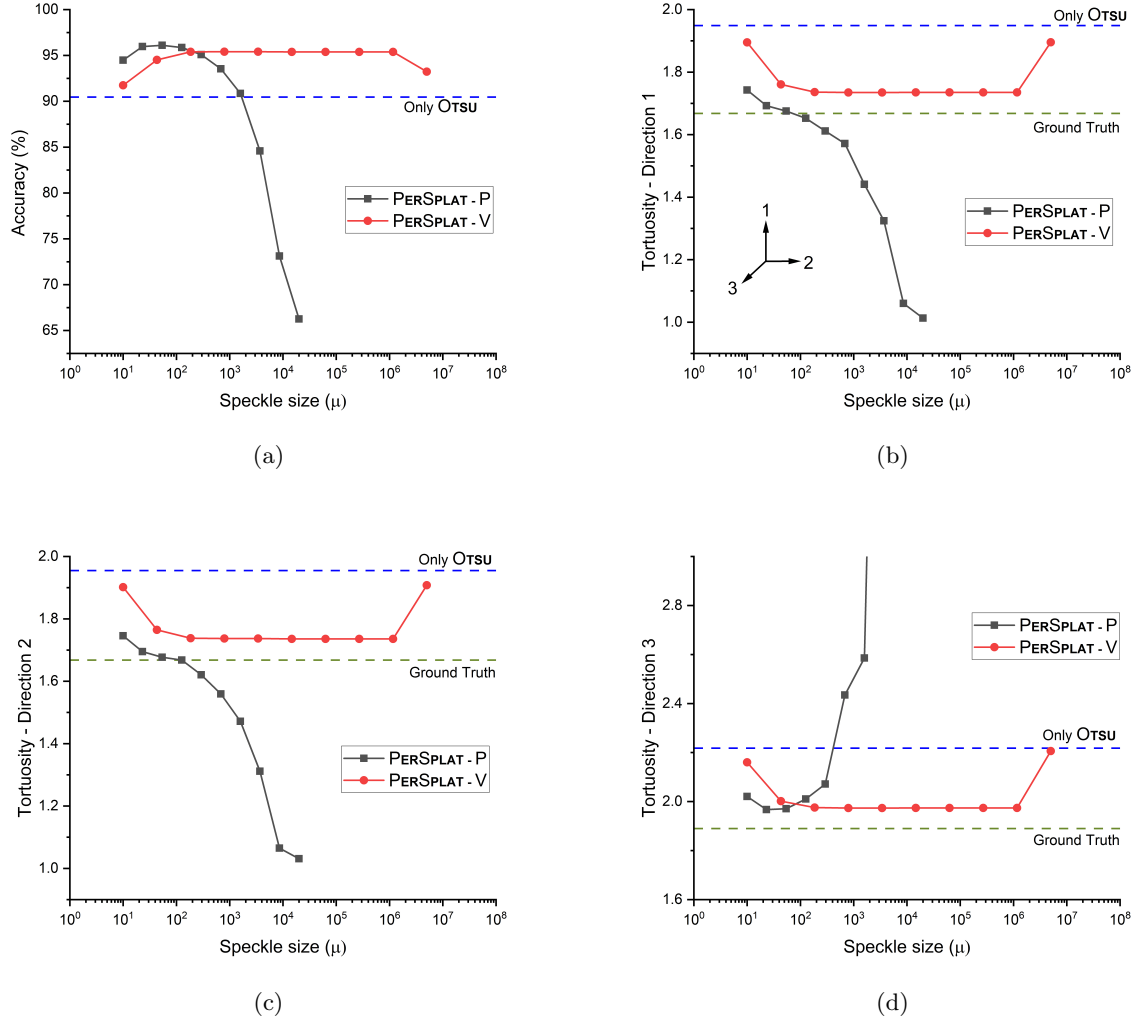


Figure 6: **Microstructure analysis with various speckle size ( $\mu$ ) parameters for PerSplat.** The input dataset is Synth1 and horizontal axes for the  $\mu$  parameter are re-scaled by logarithm function. (a) Binarization accuracy as a function of  $\mu$ . (b-d) Tortuosity as a function of  $\mu$  in the three directions.

**Varying speckle size.** Recall that with PERSPAT the user needs to choose a speckle size parameter  $\mu$  as input. To provide guidance on the parameter choosing, in Figure 6, we show how various  $\mu$  parameters impact the binarization accuracy and the calculated tortuosity; the input dataset is Synth1. Note that we chose the maximum speckle size in Figure 6 to be about 30% of the pixel/voxel count of the input, and since slices are processed independently in PERSPAT-P, the maximum  $\mu$  for PERSPAT-P is smaller than that for PERSPAT-V. From Figure 6, we observe that the change of speckle size has a more significant effect on tortuosity when using PERSPAT-P, while

tortuosity appears to be more stable at various speckle sizes when using PERSPLAT-V. This is a result of the additional dimension of connectivity introduced in 3D. To understand the phenomenon, imagine running PERSPLAT on 2D and 3D images: as the value  $s$  increases/decreases (see the description of the algorithm), the sizes of the connected components grow much faster in 3D than in 2D because of the additional dimension of connectivity. In 3D, the connected components quickly grow very large; to splat them, we need a large  $\mu$  parameter. This makes nearly the same components to be splatted for a wide range of  $\mu$  when running PERSPLAT on 3D images (PERSPLAT-V). From Figure 6, we also observe that with the right  $\mu$  (around 100), PERSPLAT-P achieved the best tortuosity values in all directions; this consistently happened in most of our experiments on synthetic datasets (some not shown in the paper).

### 3 Methods

**Software used.** MATLAB (R2019) was used to generate synthetic images, calculate binarization accuracy, and calculate tortuosity. ImageJ [32] was used for an implementation of OTSU.

**XCT Data used.** One of the microstructures used in this study is a porous polymer, Polydimethylsiloxane (PDMS). This sample was made in D.P.B’s lab using the process of templating where sugar cubes (commercial brand) were used as a template. The second sample is raw tomographic data obtained from [24] which is open-source. We performed X-ray Computed Tomography (XCT) on the porous PDMS. The sample in the open-source tomographic data is of commercially available lithium-ion batteries graphite electrode [25].

**Adding synthetic noise.** To add noise to a given ground truth image in the process of synthetic data generation, we took two steps. In step one, for each voxel from the black phase, we assign the voxel a grey-scale value based on a Gaussian distribution (for the black phase) of selected mean and variance. For voxels from the white phase, we perform similar operations. In step two, we do a simple nearest neighbor averaging of the grey-scale values. This pays attention to near-neighbor voxel value averaging that often happens at boundaries between two phases in real XCT deconvolutions – as evidenced by the broad and flat region between the two Gaussians (see Figure 1a).

**X-ray tomography.** XCT images for porous polymer (PDMS) were produced using X-ray nano-computed tomography. Computed tomography is a non-destructive technique that allows full 3D spatial density maps of an object. To gather these tomographic images, two major steps were taken. First, the sample was inserted inside a CT machine called ‘SkyScan1272’ manufactured by Bruker (Billerica, MA). A Hamamatsu L10101 micro-focus X-ray source was used with no filter. The X-ray source voltage and current was set to 40 kV and 200  $\mu$ A, respectively, to get the best scan resolution. After setting up the X-ray source, a flat field correction was updated to minimize ring artifacts. A total scan of the sample contained 1472 projection images with a length and width of 2036 pixels by 2036 pixels, respectively. Images were taken at different angles equally spaced at  $0.2^\circ$  on a scale of  $0^\circ$  to  $180^\circ$ , with exposure time of 225 ms and frame averaging of 5 per rotation. Secondly, to get 3D volume data, reconstruction of the above acquired raw data was done using a program called NRecon (Version: 1.7.4.6). The final resolution of each image was 4.50  $\mu$ m/pixel.



## 4 Conclusion

The investigation for this paper starts with an examination of the grey-scale histograms of commercial lithium-ion battery and a porous PDMS templated material. Our aim is to see how different types of histograms affect the ability of OTSU algorithm to binarize. From the binarization results, we found that some important features of the microstructure are misinterpreted due to the histogram overlap, which led to miscalculation of microstructure characteristics. To solve the problem, we designed a novel filtering algorithm called PERSPLAT based on topological persistence to rectify the small regions that are assigned to wrong group otherwise by OTSU. A tortuosity analysis showed that the ground truth values were better approximated when the data was preprocessed with PERSPLAT and then binarized, as compared to a direct binarization. The PERSPLAT algorithm has two variations when being applied on 3D data: PERSPLAT-P and PERSPLAT-V. From our analysis, we observed that PERSPLAT-V has more stability over various speckle sizes. We hope that this algorithm, in general, can make the microstructure characteristics calculations more reliable and hence help design better electrochemical devices. Additionally, this algorithm is not only limited to battery research but potentially for other applications engaging image analysis, ranging from tumor detection in biological sciences to detecting water content in geology.

## 5 Code Availability

Requests for codes that support the findings within this paper should be addressed to T.K.D (tamaldey@purdue.edu) and T.H (hou145@purdue.edu) upon reasonable request.

## 6 Data Availability

The starting 3D grey-scale XCT microstructure data files are provided in Supplemental Materials. The X-ray computed tomography data used for the analysis of porous templated polymer is publicly available online: <https://github.com/monk2k20/XCT-Polymer-Data>. The rest of the data that support the findings of this study are available from the corresponding author upon request.

## 7 Acknowledgements

The authors are grateful for support under NSF 1839267 and NSF 1839252 as well as from the Rutgers Corning/Saint-Gobain/McLaren Endowment and Purdue Start-up fund.

## 8 Author Contributions

A.V.P. fabricated the templated PDMS sample and performed XCT imaging. T.H. and T.K.D. designed the PERSPLAT algorithm and T.H. implemented the algorithm. A.V.P. and J.D.B. wrote the synthetic image generation code and the code for calculating binarization accuracy as well as performing tortuosity calculations. D.P.B. and T.K.D. provided combined supervision and guidance throughout. A.V.P. and T.H. wrote the manuscript. All authors edited the paper and approved its final version.

## 9 Competing Interests

The authors declare no competing interests.

## References

- [1] F. Marone M. Stampanonibc P. Pietsch, M. Ebner and V. Wood. Determining the uncertainty in microstructural parameters extracted from tomographic data. *Sustainable Energy Fuels*, 2(3):598–605, 2018.
- [2] J. M. Tarascon and M Armand. Issues and challenges facing rechargeable lithium batteries. In *Materials for Sustainable Energy: A Collection of Peer-Reviewed Research and Review Articles from Nature Publishing Group*, pages 171–179. 2010.
- [3] Shunsuke Yamakawa, Shingo Ohta, and Tetsuro Kobayashi. Effect of positive electrode microstructure in all-solid-state lithium-ion battery on high-rate discharge capability. *Solid State Ionics*, 344:115079, jan 2020.
- [4] Chien-Fan Chen, Ankit Verma, and Partha P. Mukherjee. Probing the Role of Electrode Microstructure in the Lithium-Ion Battery Thermal Behavior. *Journal of The Electrochemical Society*, 164(11):E3146–E3158, may 2017.
- [5] Bereket Tsegai Habte and Fangming Jiang. Effect of microstructure morphology on Li-ion battery graphite anode performance: Electrochemical impedance spectroscopy modeling and analysis. *Solid State Ionics*, 314:81–91, jan 2018.
- [6] Juan Alfonso Campos, Abhas Deva, Jarrod Lund, Aniruddha Jana, Ilenia Battiato, and R. Edwin García. Porous Electrode Phase Transition Kinetics in Li-Ion Batteries. *ECS Meeting Abstracts*, MA2020-01(1):83–83, may 2020.
- [7] L. Gireaud, S. Grugeon, S. Laruelle, B. Yrieix, and J. M. Tarascon. Lithium metal stripping/plating mechanisms studies: A metallurgical approach. *Electrochemistry Communications*, 8(10):1639–1649, oct 2006.
- [8] Xuekun Lu, Antonio Bertei, Donal P Finegan, Chun Tan, Sohrab R Daemi, Julia S Weaving, Kieran B. O’Regan, Thomas M.M. Heenan, Gareth Hinds, Emma Kendrick, Dan J.L. Brett, and Paul R Shearing. 3D microstructure design of lithium-ion battery electrodes assisted by X-ray nano-computed tomography and modelling. *Nature Communications*, 11(1), 2020.
- [9] Oluwadamilola O. Taiwo, Melanie Loveridge, Shane D. Beattie, Donal P. Finegan, Rohit Bhagat, Daniel J.L. Brett, and Paul R. Shearing. Investigation of cycling-induced microstructural degradation in silicon-based electrodes in lithium-ion batteries using X-ray nanotomography. *Electrochimica Acta*, 253:85–92, nov 2017.
- [10] Vanessa Wood. X-ray tomography for battery research and development. *NATURE REVIEWS MATERIALS*, 3(9):293–295, SEP 2018.
- [11] Tao Li, Thomas MM Heenan, Mohamad F Rabuni, Bo Wang, Nicholas M Farandos, Geoff H Kelsall, Dorota Matras, Chun Tan, Xuekun Lu, Simon DM Jacques, Dan JL Brett, Paul R Shearing, Marco Di Michiel, Andrew M Beale, Antonis Vamvakeros, and Kang Li. Design of next-generation ceramic fuel cells and real-time characterization with synchrotron X-ray diffraction computed tomography. *Nature Communications*, 10(1), 2019.

- [12] Dilip Ramani, Yadvinder Singh, Francesco P. Orfino, Monica Dutta, and Erik Kjeang. Characterization of membrane degradation growth in fuel cells using x-ray computed tomography. *Journal of The Electrochemical Society*, 165(6):F3200–F3208, 2018.
- [13] Dina Ibrahim Abouelamaiem, Guanjie He, Ivan Parkin, Tobias P. Neville, Ana Belen Jorge, Shan Ji, Rongfang Wang, Maria Magdalena Titirici, Paul R. Shearing, and Daniel J.L. Brett. Synergistic relationship between the three-dimensional nanostructure and electrochemical performance in biocarbon supercapacitor electrode materials. *Sustainable Energy and Fuels*, 2(4):772–785, mar 2018.
- [14] Seth Nickerson, Yin Shu, Danhong Zhong, Carsten Könke, and Adama Tandia. Permeability of porous ceramics by X-ray CT image analysis. *Acta Materialia*, 172:121–130, jun 2019.
- [15] Monica J. Emerson, Kristine M. Jespersen, Anders B. Dahl, Knut Conradsen, and Lars P. Mikkelsen. Individual fibre segmentation from 3D X-ray computed tomography for characterising the fibre orientation in unidirectional composite materials. *Composites Part A: Applied Science and Manufacturing*, 97:83–92, jun 2017.
- [16] Talha Qaiser, Yee Wah Tsang, Daiki Taniyama, Naoya Sakamoto, Kazuaki Nakane, David Epstein, and Nasir Rajpoot. Fast and accurate tumor segmentation of histology images using persistent homology and deep convolutional features. *Medical Image Analysis*, 55:1–14, jul 2019.
- [17] Ayyappan Nagarajan. Image processing techniques for analyzing CT scan images towards the early detection of lung cancer. *Bioinformation*, 15(8):596–599, aug 2019.
- [18] J. V. Nüchtern, M. J. Hartel, F. O. Henes, M. Groth, S. Y. Jauch, J. Haegele, D. Briem, M. Hoffmann, W. Lehmann, J. M. Rueger, and L. G. Großterlinden. Significance of clinical examination, CT and MRI scan in the diagnosis of posterior pelvic ring fractures. *Injury*, 46(2):315–319, feb 2015.
- [19] Mikayel Grigoryan, John A. Lynch, Anke L. Fierlinger, Ali Guermazi, Bo Fan, David B. MacLean, Ainsley MacLean, and Harry K. Genant. Quantitative and Qualitative Assessment of Closed Fracture Healing Using Computed Tomography and Conventional Radiography. *Academic Radiology*, 10(11):1267–1273, 2003.
- [20] Carlos Cano-Espinosa, Miguel Cazorla, and Germán González. Computer aided detection of pulmonary embolism using multi-slice multi-axial segmentation. *Applied Sciences (Switzerland)*, 10(8), 2020.
- [21] Tuan Tu Nguyen, Arnaud Demortière, Benoit Fleutot, Bruno Delobel, Charles Delacourt, and Samuel J Cooper. The electrode tortuosity factor: why the conventional tortuosity factor is not well suited for quantifying transport in porous Li-ion battery electrodes and what to use instead. *npj Computational Materials*, 6(1), 2020.
- [22] Martin Ebner, Ding Wen Chung, R. Edwin García, and Vanessa Wood. Tortuosity anisotropy in lithium-ion battery electrodes. *Advanced Energy Materials*, 4(5):1301278, apr 2014.
- [23] Nobuyuki Otsu. A threshold selection method from gray-level histograms. *IEEE Transactions on Systems, Man, and Cybernetics*, 9(1):62–66, 1979.

- [24] Patrick Pietsch and Vanessa Wood. X-Ray Tomography for Lithium Ion Battery Research: A Practical Guide. In Clarke, DR, editor, *ANNUAL REVIEW OF MATERIALS RESEARCH, VOL 47*, volume 47 of *Annual Review of Materials Research*, pages 451–479. 2017.
- [25] Simon Müller, Jens Eller, Martin Ebner, Chris Burns, Jeff Dahn, and Vanessa Wood. Quantifying Inhomogeneity of Lithium Ion Battery Electrodes and Its Influence on Electrochemical Performance. *Journal of The Electrochemical Society*, 165(2):A339–A344, 2018.
- [26] Herbert Edelsbrunner and John Harer. *Computational Topology: An Introduction*. Applied Mathematics. American Mathematical Society, 2010.
- [27] Antoni Buades, Bartomeu Coll, and Jean-Michel Morel. A review of image denoising algorithms, with a new one. *Multiscale Modeling & Simulation*, 4(2):490–530, 2005.
- [28] Christos P. Loizou and Constantinos S. Pattichis. Despeckle filtering algorithms and software for ultrasound imaging. *Synthesis lectures on algorithms and software in engineering*, 1(1):1–166, 2008.
- [29] Herbert Edelsbrunner, David Letscher, and Afra Zomorodian. Topological persistence and simplification. In *Proceedings of the 41st Annual Symposium on Foundations of Computer Science*, pages 454–463. IEEE, 2000.
- [30] P. Pietsch, M. Ebner, F. Marone, M. Stampanoni, and V. Wood. Determining the uncertainty in microstructural parameters extracted from tomographic data. *Sustainable Energy and Fuels*, 2(3):598–605, mar 2018.
- [31] S. J. Cooper, A. Bertei, P. R. Shearing, J. A. Kilner, and N. P. Brandon. TauFactor: An open-source application for calculating tortuosity factors from tomographic data. *SoftwareX*, 5:203–210, jan 2016.
- [32] Johannes Schindelin, Ignacio Arganda-Carreras, Erwin Frise, Verena Kaynig, Mark Longair, Tobias Pietzsch, Stephan Preibisch, Curtis Rueden, Stephan Saalfeld, Benjamin Schmid, et al. Fiji: An open-source platform for biological-image analysis. *Nature methods*, 9(7):676–682, 2012.